ARTICLE

Nanoimprint-Assisted Shear Exfoliation (NASE) for Producing Multilayer MoS_2 Structures as Field-Effect Transistor Channel Arrays

Mikai Chen,[†] Hongsuk Nam,[†] Hossein Rokni,[†] Sungjin Wi, Jeong Seop Yoon, Pengyu Chen, Katsuo Kurabayashi, Wei Lu, and Xiaogan Liang*

Department of Mechanical Engineering, University of Michigan, Ann Arbor, Michigan 48109, United States. [†]M.C., H.N., and H.R. contributed equally.

ABSTRACT MoS_2 and other semiconducting transition metal dichalcogenides (TMDCs) are of great interest due to their excellent physical properties and versatile chemistry. Although many recent research efforts have been directed to explore attractive properties associated with MoS_2 monolayers, multilayer/few-layer MoS_2 structures are indeed demanded by many practical scale-up device applications, because multilayer structures can provide sizable electronic/photonic state densities for driving upscalable electrical/optical signals. Currently there is a lack of processes capable of producing ordered, pristine multilayer structures of MoS_2 (or other relevant TMDCs) with manufacturing-grade uniformity of thicknesses and electronic/photonic properties. In this article, we present a nanoimprint-based approach toward addressing this challenge. In this approach, termed as nanoimprint-assisted shear exfoliation (NASE), a prepatterned bulk MoS_2 stamp is pressed into a polymeric fixing layer, and the imprinted MoS_2 features are exfoliated along a shear direction. This shear exfoliation can significantly enhance the exfoliation efficiency and thickness uniformity of exfoliated flakes in comparison with previously reported exfoliation processes. Furthermore, we have preliminarily demonstrated the fabrication of multiple transistors and biosensors exhibiting excellent device-to-device performance consistency. Finally, we present a molecular dynamics modeling analysis of the scaling behavior of NASE. This work holds significant potential to leverage the superior properties of MoS_2 and other emerging TMDCs for practical scale-up device applications.

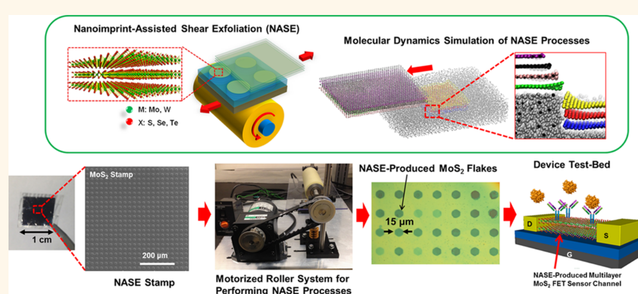

KEYWORDS: nanoimprint · nanoprint · nanomechanics · MoS_2 · electronics · transistor

Atomically layered transition metal dichalcogenides (TMDCs) (*e.g.*, WSe_2, WS_2, and MoS_2) have emerged as attractive material candidates for making novel functional devices. Especially, MoS_2 exhibits excellent electronic, photonic, and mechanical properties, as well as good compatibility to planar nanofabrication processes, potentially enabling low-cost mass production of MoS_2-based products in the near future.[1-5] Researchers have demonstrated a series of new prototype devices based on MoS_2 and other relevant TMDC materials in their laboratories, such as high-performance thin-film transistors (TFTs),[1,6,7] highly sensitive chemical/biological sensors,[8-10] phototransistors,[11] multibit nonvolatile transistor memories,[12] and photovoltaic (PV) devices with high quantum efficiencies, *etc.*[13-15] To leverage the superior electronic/photonic characteristics of such devices for practical scale-up applications, the research community currently needs new nanomanufacturing methods capable of producing MoS_2 device arrays with deterministic and uniform properties.

A great deal of recent research effort focuses on the attractive properties associated with monolayer MoS_2 structures. These properties include direct bandgaps, which are suitable for light-emitting applications,[2] strong valley-selective circular dichroism, which can potentially enable future low-energy-dissipation valleytronic devices,[16,17] as well as atomic scale thicknesses that represent the ultimate scaling of

* Address correspondence to xiaoganl@umich.edu.

Received for review March 20, 2015 and accepted August 22, 2015.

Published online August 24, 2015
10.1021/acsnano.5b01715

© 2015 American Chemical Society

material dimension in the vertical direction and can potentially enable miniaturization of electronic devices beyond Moore's Law.[18] Therefore, many material-synthesis-oriented works seek to product MoS_2 monolayers over large areas.[19−21] In spite of these intensive efforts related to monolayers, many important nanoelectronic/optoelectronic applications, such as transistor-based memories/sensors,[9,10,12] photovoltaics,[14,15,22] and power switching TFTs,[23] indeed demand high-quality multilayer MoS_2 structures. Multilayer structures can provide excellent transport properties (*e.g.*, relatively high carrier mobility) and sizable densities/amounts of electronic/photonic states, enabling device applications that need to drive large current/voltage signals or absorb a large amount of photons.[23,24] However, there are so far very few research efforts dedicated to produce high-quality multilayer MoS_2 device structures with a high uniformity of thickness as well as electronic/photonic properties over large areas.

Toward ultimately realizing upscalable production of highly uniform multilayer MoS_2 device arrays or large-scale circuits, in this work we created and studied a top-down nanofabrication approach capable of producing pristine multilayer MoS_2 flake arrays with high uniformity of flake thicknesses (*i.e.*, relative thickness error ∼12%) over cm^2-scale areas, and also demonstrated multiple working transistors and electronic biosensors made from as-produced MoS_2 flakes, which exhibited consistent performance as well as a good uniformity in the critical device performance parameters. Specifically, in this presented nanofabrication process, termed as nanoimprint-assisted shear exfoliation (NASE), multilayer MoS_2 structures prepatterned on a bulk MoS_2 stamp were imprinted into a polymeric fixing layer and subsequently exfoliated along a shear direction using a motor-driven roller tool. As compared to previously reported exfoliation methods for generating layered materials,[25,26] NASE can result in significantly improved transfer efficiency of prestructured MoS_2 features as well as uniformity of resultant flake thicknesses. Our transistor-based biosensors made from NASE-produced MoS_2 flakes exhibited a high device-to-device consistency in the sensor responses to specific biomarkers. We have preliminarily demonstrated quantification of a standard curve for tumor necrosis factor-alpha (TNF-α) detection by using multiple such biosensors. Furthermore, our molecular dynamics (MD) modeling analysis showed that the NASE process can be potentially used for generating 2-D layer device structures with nanoscale lateral dimensions.

RESULTS AND DISCUSSION

Figure 1 illustrates our NASE method for producing multilayer MoS_2 flake arrays with uniform thicknesses. In a NASE process, first a bulk MoS_2 ingot is prestructured with protrusive multilayer mesa arrays by using photolithography followed with plasma etching (Figure 1 (a)). After this process, this ingot becomes a bulk MoS_2 stamp. More details about the MoS_2 stamp fabrication have been reported in our previous work.[26] Here, the height of protrusive mesas can be well controlled by adjusting the plasma etching duration. This mesa height will determine the imprint depth (d_{NIL}) resulted by the stamp.[27] When the stamp is ready, a substrate (*e.g.*, glass, Si, or SiO_2) is spin-coated with a polymeric fixing layer (*e.g.*, thermoplastics or cross-linkable polymers), and the MoS_2 stamp is subsequently pressed into the fixing layer on the substrate through a nanoimprint lithography (NIL) process (Figure 1 (b)). Afterward, a lab-made motorized roller

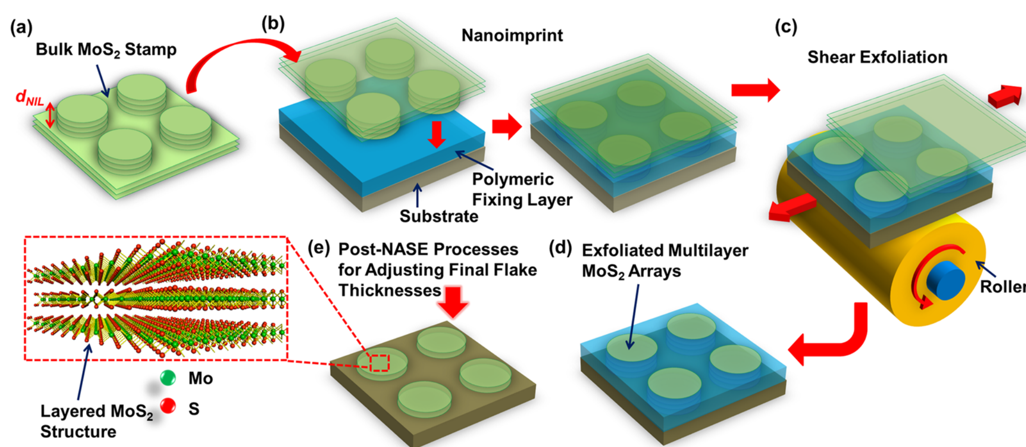

Figure 1. Illustration of nanoimprint-assisted shear exfoliation (NASE) for producing few-layer/multilayer MoS_2 device structure arrays: (a) fabrication of a bulk MoS_2 stamp bearing protrusive device features; (b) nanoimprint process for pressing the protrusive features on the bulk MoS_2 stamp into a polymeric fixing layer coated on a substrate; (c) exfoliation of imprinted MoS_2 features along a shear direction, which is actuated by a motorized roller tool; (d) multilayer MoS_2 flakes imprinted/exfoliated by NASE, which are expected to exhibit a high uniformity in thickness as well as electronic properties; (e) post-NASE processes for further adjusting the final thicknesses of exfoliated MoS_2 flakes to meet various device application requirements.

tool is used to displace the MoS_2 stamp along the substrate surface (*i.e.*, a shear direction). Due to the shear displacement, the multilayer MoS_2 mesas already imprinted into the fixing layer can be exfoliated away from the bulk stamp (Figure 1 (c)). The thicknesses of exfoliated multilayer flakes are anticipated to be mainly determined by the imprint depth (d_{NIL}) (Figure 1 (d)). In comparison with previously reported exfoliation methods for generating layered materials, such as electrostatic exfoliation,[28,29] plasma-assisted nanoprinting,[26] and mechanical cutting/transfer-printing,[25] the unique shear exfoliation mechanism involved in NASE can result in significantly improved transfer-printing efficiency of prestructured MoS_2 features as well as higher uniformity of exfoliated MoS_2 feature thicknesses. In comparison with chemical synthesis approaches for generating multilayer MoS_2, NASE is expected to be able to produce MoS_2 structures with larger average crystal domain size (10s−100s μm), higher ordering of interlayer stacking configurations,[30,31] and therefore better transport properties.[14,19−21] Furthermore, NASE could be further generalized for producing high-quality multilayer structures of other atomically layered materials, such as highly ordered pyrolytic graphite (HOPG) and emerging topological insulators (*e.g.*, Bi_2Se_3 and Bi_2Te_3). After a NASE process, additional etching/ablation processes could be subsequently used for further adjusting the thicknesses of NASE-produced MoS_2 flakes to meet the requirements of various device applications (Figure 1 (e)),[32,33] such as monolayers for light-emitting devices,[2] 10−50 nm thick flakes for making high-mobility transistors,[23,24,34−36] and 50−200 nm flakes for photovoltaic/photodetection devices.[13−15] There have been several works seeking to control MoS_2 layer thickness. For example, Liu *et al.* recently successfully demonstrated layer-by-layer thinning of multilayer MoS_2 structures down to monolayers by using Ar^+ plasma.[32] Especially, Liu *et al.*'s high-resolution transmission electron microscopy (HRTEM) results showed that Ar^+ plasma irradiation does not affect the bottom layer before totally removes the top-layer MoS_2 atoms.[32] Such a layer-wise etching mechanism is attributed to the strong bonding strength of the S−Mo−S structure and the relatively weak interlayer interaction.[32] In addition, Castellanos-Gomez *et al.* developed a laser thinning method, which can also deterministically thin multilayer MoS_2 down to a single layer.[33] In particular, this technique relies on the sublimation of the upper layers, which is caused by the laser-induced heating.[33] By choosing an appropriate laser power density, this process can have a self-termination mechanism; *i.e.*, the bottom layer remains on the substrate after all upper layers are totally removed because the bottom layer is in direct contact with the Si substrate that acts as a heat sink and effectively suppresses the sublimation of the bottom layer.[33]

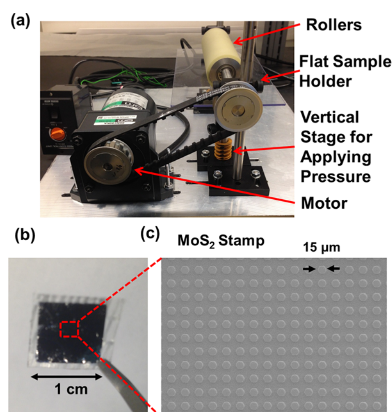

Figure 2. Photographs of (a) the motorized roller tool for performing NASE processes and (b) an exemplary 1 cm-size MoS_2 stamp. (c) shows the SEM image of this stamp, which bears 40 nm-high, 15 μm-size protrusive mesa (or pillar) arrays.

Figure 2 (a) shows a photograph of our lab-made motorized roller tool for performing the shear exfoliation of multilayer MoS_2 structures. This tool consists of an AC brushless motor with an electric speed controller, a flat sample holder for immobilizing either the stamp or the substrate, a motor-driven roller for generating the relative shear displacement between the stamp and the substrate, and a vertical stage for applying a gauge pressure to maintain the stamp flat during the shear exfoliation. In particular, the web speed of the roller surface can be adjusted in the range of 0−3 cm/s. The vertical stage bearing a set of coil springs can generate an adjustable gauge pressure (0−0.5 MPa) for firmly pressing the MoS_2 stamp against the substrate, therefore effectively avoiding the formation of wrinkles in exfoliated MoS_2 layers. The supplementary video in the Supporting Information demonstrates a shear exfoliation process driven by our roller tool.

In this work, we chose MoS_2 as the test-bed material for investigating NASE processes, because (i) MoS_2 is the most widely studied TMDC material; (ii) MoS_2 and other TMDCs share very similar mechanical properties, which makes the nanofabrication processes developed in this work generally applicable to all other TMDCs and layered materials. Figure 2 (b) and (c) display an optical micrograph (OM) and a scanning electron micrograph (SEM) of an exemplary MoS_2 stamp prestructured with 40 nm high, 15 μm size pillar arrays, respectively. The size of the whole stamp is ~1 cm. More details related to the roller tool, the fabrication of bulk MoS_2 stamps, and the NASE processes are described in the Materials and Methods.

Figure 3 (a) shows four optical micrographs of NASE-produced MoS_2 flakes, which were exfoliated into a 55 nm thick polystyrene (PS) fixing layer coated on a SiO_2/Si substrate (SiO_2 thickness, 300 nm). These micrographs were captured from different locations over the whole NASE-processed area (~1 cm^2), as mapped in the inset photograph of the whole NASE

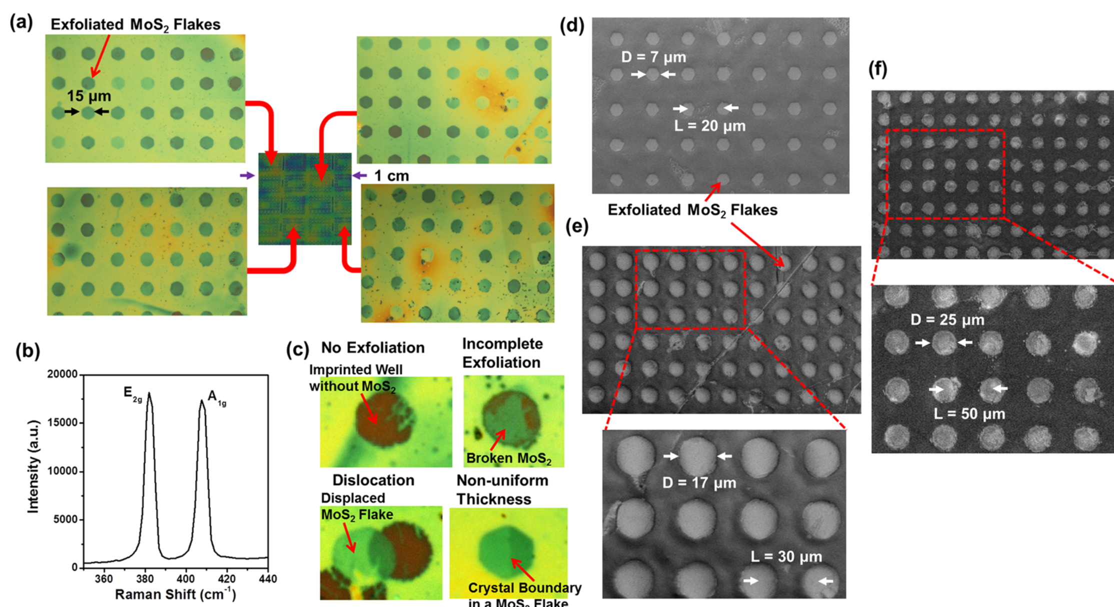

Figure 3. NASE results: (a) four optical micrographs of MoS_2 flake arrays imprinted/exfoliated into a PS fixing layer coated on a SiO_2/Si substrate by using NASE, which were captured from different locations over the whole NASE-processed area (~1 cm^2), as mapped in the inset photograph of the whole NASE sample; (b) Raman spectrum of an exemplary multilayer MoS_2 flake; (c) optical micrographs of typical imperfections that occur in NASE. (d–f) SEM images of a set of NASE-produced arrays of multilayer MoS_2 flakes with various flake diameters (*D*) and flake-to-flake spacings (*L*). For all of these samples, the imprint depth (d_{NIL}) is ~50 nm.

sample. Raman spectroscopy was performed to identify the existence of exfoliated MoS_2 flakes in the imprinted PS layer. Our Raman results show that more than 80% of imprinted wells in the PS fixing layer have MoS_2 flakes. Figure 3 (b) shows a typical Raman spectrum of a NASE-produced MoS_2 flake, which exhibits two characteristic peaks, A_{1g} and E_{2g}, corresponding to the out-of-plane and in-plane vibration modes of MoS_2 layers, respectively.[37] For all NASE-produced MoS_2 flakes, their $A_{1g}-E_{2g}$ peak spacings are larger than 19 cm^{-1}. This indicates that all NASE-produced flakes are multilayer MoS_2 structures.[38] Our OM and Raman characterizations show that NASE can produce orderly arranged multilayer MoS_2 device structures over cm^2-scale areas. Although most imprinted well pixels in PS fixing layers have high-quality MoS_2 flakes faithfully exfoliated from the bulk stamps, observable imperfection features still occur during NASE processes. Figure 3 (c) displays the OM images of typical imperfection features occurring in NASE, which includes (i) imprinted PS wells without MoS_2 (*i.e.*, no exfoliation), (ii) imprinted wells with broken MoS_2 fragments (*i.e.*, incomplete exfoliation), (iii) MoS_2 dislocated away from the imprinted PS wells, and (iv) nonuniform thickness distribution within individual flakes. The occurring probabilities of these imperfection features may be relevant to mechanical properties of TMDC stamps and polymeric fixing layers, flatness/total size of TMDC stamps, geometric dimensions of prestructured TMDC structures, and NASE processing parameters (*e.g.*, roller speed and vertical pressure), *etc.* Especially, we found that the aspect ratio (*i.e.*, the ratio of the height to the lateral size of a feature) of protrusive mesas prestructured on TMDC stamps greatly affects the quality of NASE-produced flakes. In particular, given a fixed lateral size of mesas of 15 μm, our current NASE system can easily exfoliate 40–200 nm high MoS_2 mesas without resulting in significant imperfections. However, when the initial mesa thickness (or height) is thinner than 40 nm, the occurring probability of broken, wrinkled, and dislocated mesa flakes is significantly increased. Therefore, as mentioned above, the better route for producing 0.7–40 nm thick, 15 μm size MoS_2 flake arrays (*i.e.*, monolayer to 60-layer structures) is to employ NASE for producing uniform flake arrays thicker than 40 nm, and subsequently perform a post-NASE etching process to thin the NASE-produced flakes. For example, Liu *et al.* has demonstrated layer-by-layer thinning of multilayer MoS_2 structures.[32] This thinning approach in combination with NASE can potentially produce MoS_2 structure arrays with arbitrary thicknesses for meeting the requirements of various device applications. More nanomechanics-oriented works will be performed in the future to fully understand the role of other factors in generating imperfections during NASE processes and optimize the processing conditions to eliminate the imperfection features displayed in Figure 3 (c).

To study the effect of the lateral dimensions of MoS_2 mesas on the quality of NASE-produced flake arrays, we also produced MoS_2 flake arrays with different lateral dimensions. Figure 3 (d–f) display the SEM images of a set of NASE-produced arrays of multilayer MoS_2 flakes with various flake diameters (*D*) and

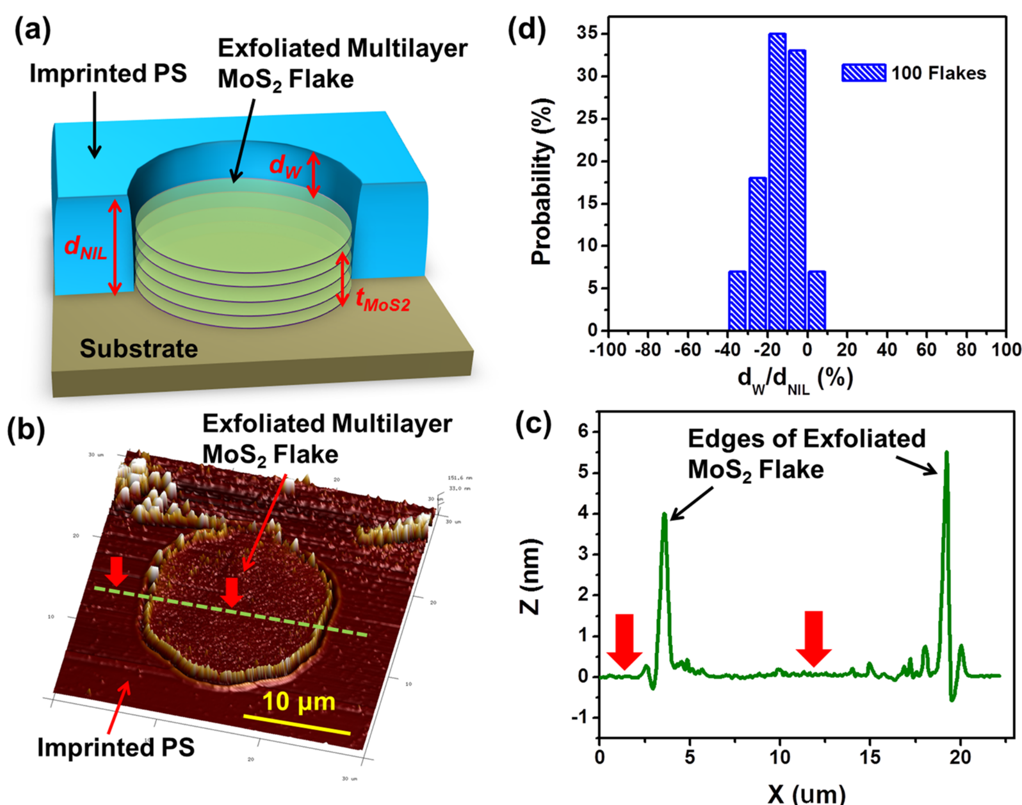

Figure 4. AFM characterization of NASE-produced MoS_2 flakes exfoliated into a PS fixing layer: (a) schematic of a multilayer MoS_2 flake with thickness of t_{MoS2} exfoliated into an imprinted PS well with imprint depth of d_{NIL}, resulting in an effective well depth of d_W; (b) an exemplary 3-D AFM image of a multilayer MoS_2 flake exfoliated into an imprinted PS well; (c) an AFM scanline extracted from the AFM image shown in (b) (*i.e.*, the dashed line shown in (b)), from which the d_W value of this MoS_2-embeded well can be measured from the topographic difference between locations denoted with arrows; (d) statistics of d_W/d_{NIL} data measured from 100 MoS_2-embeded wells, which shows that the standard deviation of d_W/d_{NIL} data (or the relative thickness error of NASE-produced multilayer MoS_2 flakes) is estimated to ~12%.

flake-to-flake spacings (L) (*i.e.*, (d) $D = 7$ μm, $L = 20$ μm; (e) $D = 17$ μm, $L = 30$ μm; (f) $D = 25$ μm, $L = 50$ μm). For all of these samples, the imprint depth (d_{NIL}) is ~50 nm. The flake arrays with D = 7 and 17 μm exhibit very similar quality as compared to 15 μm size ones shown in Figure 3 (a). Especially, most flakes in these arrays have relatively smooth top surfaces, as shown in Figure 3 (d) and (e). Figure 3 (f) shows that the NASE-produced array with $D = 25$ μm also exhibits a comparable yield (~80%) of exfoliated MoS_2 flakes, but the top surfaces of these 25 μm size flakes exhibit a noticeably larger roughness in comparison with those of the flakes with the smaller D values. This is attributed to the relatively low aspect-ratio (*i.e.*, d_{NIL}/D) of these 25 μm size flakes, which results in relatively low flake rigidity and therefore a high occurring probability of wrinkled MoS_2 layers. In this work, we found that the quality of NASE-produced flakes is not sensitive to the flake spacing (L) or density. The relationship between the flake rigidity and the occurring probability of wrinkling in exfoliated layers is further discussed below based on our molecular dynamics (MD) simulations.

Because NASE-produced MoS_2 flakes are embedded into PS fixing layers, their thicknesses cannot be directly measured by using atomic force microscopy (AFM) or the color coding method.[39] Especially, it should be noted that our MoS_2 flakes, under OM illumination, exhibit varying colors ranging from green to deep blue, as demonstrated in Figure 3 (a). Such a color variation among MoS_2 flakes are mainly attributed to the spatial variation of the PS film thickness or the residual layer thickness (RLT), which are caused by the nonflatness of our current MoS_2 stamps (or current commercially available MoS_2 ingots). Therefore, such a color variation does not correctly indicate the thickness distribution among exfoliated MoS_2 flakes. To evaluate the uniformity of NASE-produced MoS_2 flake thicknesses, we employed AFM to measure the effective well depth (d_W) of imprinted PS wells bearing exfoliated MoS_2 layers, as illustrated in Figure 4 (a). The d_W value of a MoS_2-embeded well is assumed to be the difference between the imprint depth (d_{NIL}, or the initial height of MoS_2 mesas prestructured on the stamp) and the thickness (t_{MoS2}) of the MoS_2 flake embedded inside this well. Figure 4 (b) shows a 3-D AFM image of an exemplary NASE-produced MoS_2 flake exfoliated into an imprinted PS well. The dashed line indicates an AFM scanline that is replotted in Figure 4 (c). The d_W value of this MoS_2-embeded well is measured from the topographic difference between

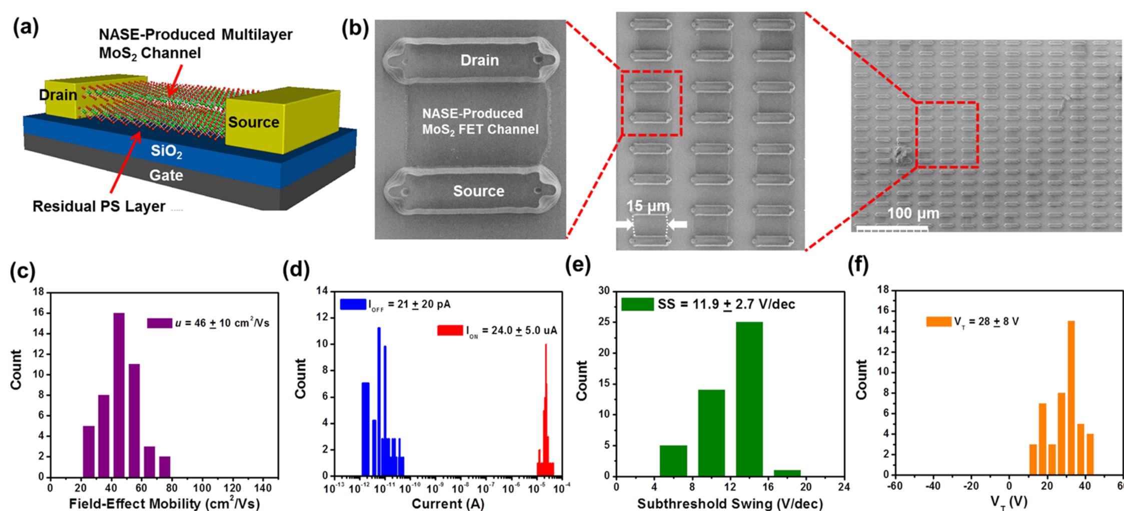

Figure 5. Back-gated FET arrays made from NASE-produced MoS_2 flakes: (a) Schematic illustration of a back-gated MoS_2 FET. (b) SEM images of a representative FET array made from the multilayer MoS_2 flakes (thickness ∼20 nm) produced in a NASE process. For all FETs, the channel width (W) and length (L) are 15 and 10 μm, respectively; the back gate dielectric is 300 nm SiO_2 + residual PS (estimated to be thinner than 5 nm). The following graphs display the statistics of (c) mobility (μ), (d) On/Off currents (I_{ON} and I_{OFF}), (e) subthreshold swing (SS), and (f) threshold voltage (V_T) data measured from 45 MoS_2 FETs fabricated by a NASE process. Figure S1 in the Supporting Information lists the transfer characteristics of these 45 FETs.

the center of this MoS_2 flake and a location outside the well, as indicated by the red arrows in Figure 4 (c). For this specific imprinted well, d_W is measured to be ∼0, indicating that $t_{MoS2} \sim d_{NIL}$ = 40 nm. Figure 4 (d) displays the statistics of d_W/d_{NIL} values measured from 100 imprinted wells bearing MoS_2 flakes. These structures were produced in a single NASE process. Figure 4 (d) shows that the standard deviation of d_W/d_{NIL} data (or the relative thickness error of NASE-produced multilayer MoS_2 flakes) is estimated to ∼12%. This relative thickness error is much smaller than those of multilayer structures produced by previously reported exfoliation methods.[25,26,28,29,40]

To evaluate the uniformity of the electronic properties of multilayer MoS_2 flakes produced by NASE, we fabricated back-gated field-effect transistor (FET) arrays with NASE-produced MoS_2 channels and obtained the statistical data of the transfer characteristics of multiple FETs. Figure 5 (a) schematically illustrates the FET structure. Figure 5 (b) shows the SEM images of a representative FET array made from the multilayer MoS_2 flakes produced in a NASE process. For all as-fabricated FETs, the channel width (W) and length (L) are 15 and 10 μm, respectively; the MoS_2 channel thickness is around 20 nm; the back-gate dielectric consists of a 300 nm thick thermally grown SiO_2 layer plus a residual PS layer. Here, the residual PS thickness ($t_{residual}$) under each MoS_2 channel is estimated to be thinner than 5 nm by using $t_{residual} = t_{PS} - d_{NIL}$, in which t_{PS} is the initial PS layer thickness before the NASE process. More details about the fabrication of MoS_2 FET arrays can be found in the Materials and Methods.

Here, it should be noted that our current post-NASE FET fabrication process is yet to be optimized and it usually results in the peeling of part of the NASE-produced MoS_2 flakes. This is because of the poor adhesion between layered materials and most of substrate materials. This issue is not only for NASE-produced MoS_2 samples, but also generally for all 2D layered materials. Exploring the ultimate solution to this problem is underway but still beyond the scope of the present work. Fortunately, in our work, the survived MoS_2 flakes remain staying at their original locations in the array, and the yields of working FETs over cm^2-scale areas are typically 50−60% (the yield of NASE-produced MoS_2 flakes is ∼80%). Such samples are sufficiently good for providing a number of FETs for evaluating the uniformity of the electronic properties of NASE-produced MoS_2 flakes.

Figure S1 in the Supporting Information displays the transfer characteristics (*i.e.*, drain-source current (I_{DS}) − gate voltage (V_G) curves measured under a given drain-source voltage (V_{DS} = 1 V)) across 45 FETs. These FETs were made from the multilayer MoS_2 flakes produced in a NASE process and distributed over a 1 cm^2 area. Figure 5 (c−f) show the statistics of field-effect mobility (μ), On/Off currents (I_{ON} is the I_{DS} measured at V_G = 60 V; I_{OFF} is the minimum value of I_{DS} within the V_G range of ±60 V), subthreshold swing (SS), and threshold voltage (V_T) data, which were extracted from the transfer characteristic curves of these 45 FETs. Specifically, the mean values of μ, I_{ON}, I_{OFF}, SS, and V_T were statistically measured to be μ = 46 ± 10 cm^2/(V s), I_{ON} = 24.0 ± 5.0 μA (or, 1.60 ± 0.33 μA per 1 μm channel width), I_{OFF} = 21 ± 20 pA, SS = 11.9 ± 2.7 V/dec, and V_T = 28 ± 8 V, respectively. First, it should be noted that the relatively large SS values of our FETs are attributed to the relatively thick back-gate dielectric (*i.e.*, 300 nm SiO_2) used here, and such SS values could be significantly reduced by using much thinner dielectrics.

The I_{OFF} data of our FETs exhibit a much larger relative standard deviation (~95%) as compared to other parameters, which is mainly attributed to the measurement precision (2−10 pA) of our semiconductor analyzer. The quantity V_T could have zero or negative values, and therefore the relative standard deviation of V_T data is meaningless for evaluating the uniformity of our FETs. Therefore, we specifically use the relative standard deviations of μ, I_{ON}, and SS data for evaluating the uniformity. The relative standard deviations of these parameters range from 21 to 23%. This shows that even though our post-NASE FET fabrication process is yet to be optimized, our current FET arrays made from NASE-produced multilayer MoS_2 flakes already exhibit a good uniformity in critical FET parameters. The observed variances in the performance parameters of our FETs are mainly attributed to several possible factors, including (1) the device-to-device variance in the residual PS layer thicknesses; (2) the NASE-introduced defects, as discussed above (Figure 3 (c)); (3) the contaminants introduced during the post-NASE FET fabrication processes; (4) intrinsic nonuniformity of the material properties of initial MoS_2 ingots (*e.g.*, crystal orientations, domain size distributions, and intrinsic defects).

To evaluate the effect of the residual PS layers on the uniformity of the electronic properties of NASE-produced MoS_2 flakes, we used another process to make MoS_2 FETs free of the residual PS. To make such FETs, a SiO_2-coated p^+-Si substrate bearing NASE-produced MoS_2 flakes was soaked in toluene for 1−2 h. Until this step, the sample had not been subjected to any plasma etching. Therefore, the imprinted PS on the substrate (including the residual PS layers under MoS_2 flakes) was able to be completely removed because there is no cross-linking in PS. However, this cleaning process displaced (and even peeled) many MoS_2 flakes and only a few survived MoS_2 flakes were chosen for making FETs. Because the selected MoS_2 flakes had been shifted away from their original array configurations, we had to perform repetitive lithography, metal deposition, and lift-off processes for making multiple FETs. In particular, special finger contacts (5 nm Ti/50 nm Au) were fabricated to access to individual selected MoS_2 flakes. This was a time-consuming task and resulted in a much lower device yield as compared to the method, discussed above, for making FET arrays with the residual PS. Figure S2 in the Supporting Information displays two representative back-gated FETs made from multilayer MoS_2 flakes that were cleaned by Toluene. Figure S3 shows the transfer characteristics of 11 such FETs made from PS-free multilayer MoS_2 flakes, and Figure S4 displays the statistics of (a) mobility (μ), (b) On/Off currents (I_{ON} and I_{OFF}), (c) subthreshold swing (SS), and (d) threshold voltage (V_T) data measured from these 11 FETs. For the following discussion, these FETs are referred to as PS-free FETs, and the FETs in the arrays (*i.e.*, those shown in Figure 5) are referred to as PS-retained FETs.

First, our device characterization shows that the field-effect mobility data measured from our PS-retained FETs (*i.e.*, $\mu = 46 \pm 10$ cm^2/(V s)) have a slightly smaller mean value and a slightly larger standard deviation in comparison with those measured from our PS-free FETs (*i.e.*, $\mu = 53 \pm 7$ cm^2/(V s)). This slight difference is attributed to the roughness scattering at the MoS_2/PS interface, which could slightly reduce the field effect mobility of the multilayer MoS_2 FET and broaden the dispersion of the mobility values measured from different FETs. Because such a PS-induced mobility reduction is estimated to be only ~13%, we can think that the presence of residual PS between multilayer MoS_2 flakes and SiO_2 gate dielectrics does not result in a detrimental damage to the mobility property of multilayer MoS_2 FETs. In comparison with our PS-retained FETs, our PS-free FETs exhibit a smaller average SS (*i.e.*, SS = 8.4 ± 1.1 V/dec for PS-free FETs, whereas SS = 11.9 ± 2.7 V/dec for PS-retained ones). This difference is attributed to that the residual PS layer under a MoS_2 FET channel introduces an additional capacitor connected with the SiO_2 capacitor in series, which decreases the overall gate dielectric capacitance and therefore increases the SS value of this FET. In addition, the relative standard deviation of the SS data measured from PS-retained FETs (~23%) is noticeably larger than that measured from PS-free FETs (~13%). This is attributed to the nonuniformity of the residual PS layer thicknesses under NASE-produced MoS_2 flakes, which may introduce an additional nonuniformity in back-gate capacitances and hence the SS data of PS-retained FETs. In comparison with PS-free FETs, the PS-retained FETs have statistically more positive V_T values (*i.e.*, $V_T = -27 \pm 10$ V for PS-free FETs, whereas $V_T = 28 \pm 8$ V for PS-retained ones). This difference is attributed to the polymer-induced surface-charge-transfer (SCT) doping (p-type doping) in MoS_2 channels.

Our MoS_2 FETs can be further implemented as label-free electronic biosensors for quantifying specific biomolecules. In this work, we specifically demonstrated quantification of a standard curve for tumor necrosis factor-alpha (TNF-α), a cell signaling protein involved in systemic inflammation caused by human diseases, by using multiple MoS_2 FET biosensors. Figure 6 (a) illustrates a MoS_2 FET sensor functionalized with anti-human TNF-α antibody receptors for detecting TNF-α molecules. The details about electrode passivation, antibody functionalization, and TNF-α detection are described in the Materials and Methods. To realize quantitative immunoassay, multiple sensors with consistent sensor responses to specific analyte concentrations are needed. We choose the relative change of ON-state I_{DS} under a fixed set of V_G and V_{DS}, *i.e.*, $R = (I_{DS(anti)} - I_{DS})/I_{DS}$, as the sensor response quantity.

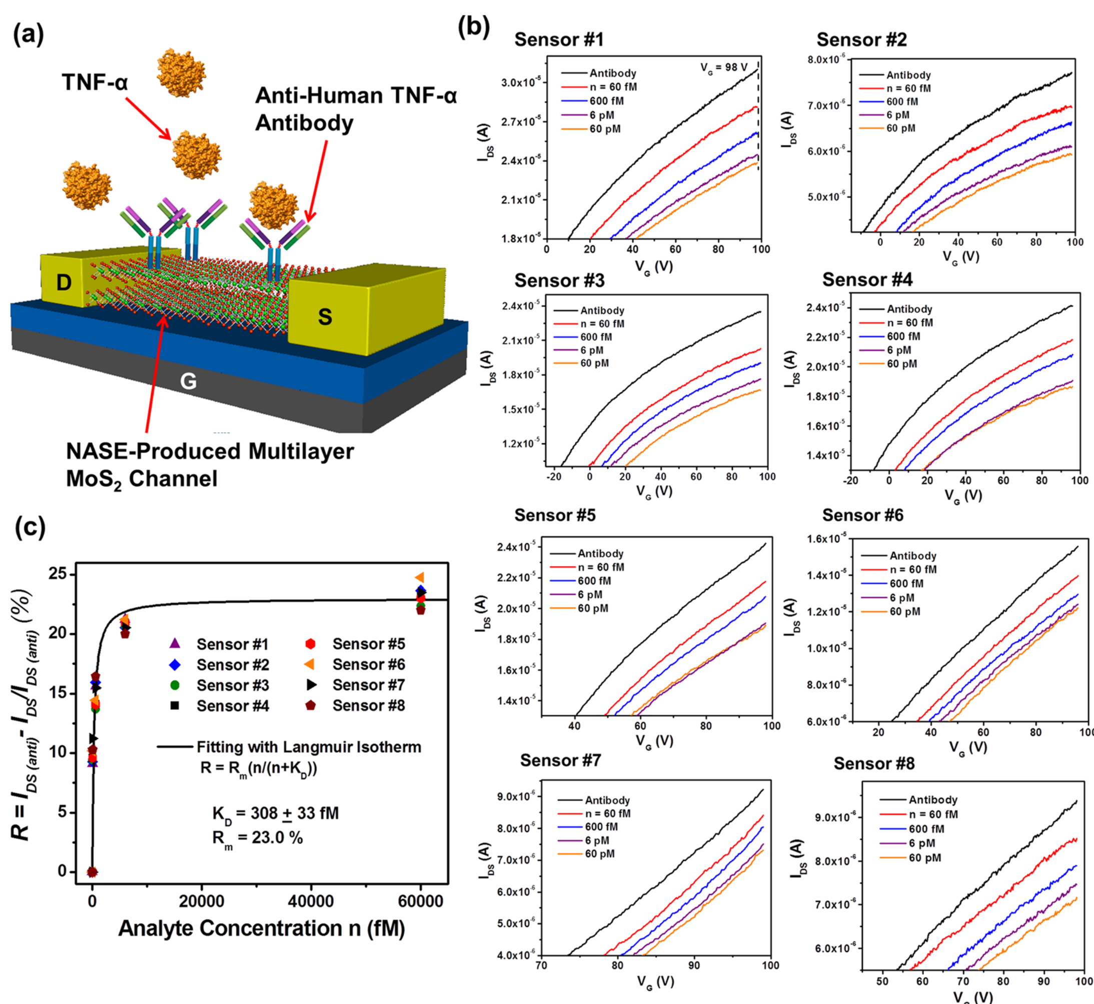

Figure 6. MoS_2 transistor biosensors made from NASE-produced multilayer MoS_2 flakes: (a) illustration of a MoS_2 transistor biosensor, in which antihuman TNF-α antibodies are directly functionalized on the MoS_2 transistor channel; (b) sensor responses (*i.e.*, transfer characteristics) to various TNF-α concentrations (*i.e.*, *n* = 0, 60 fM, 600 fM, 6 pM, and 60 pM) measured from eight different sensors; (c) calibrated responses (*i.e.*, relative change of ON-state I_{DS} measured at a fixed V_G = 98 V) with respect to *n*, measured from difference sensors, which exhibit a high degree of device-to-device consistency and can be well fitted with Langmuir isotherm.

Here, $I_{DS(anti)}$ refers to the ON-state I_{DS} measured from an as-functionalized sensor (*i.e.*, TNF-α concentration $n = 0$). Figure 6 (b) shows the transfer characteristics of eight sensors measured under a set of incremental TNF-α concentrations (*i.e.*, *n* = 0, 60 fM, 600 fM, 6 pM, and 60 pM). The sensor responses (*i.e.*, values of $R = (I_{DS(anti)} - I_{DS})/I_{DS}$) were extracted at a fixed V_G = 98 V (*i.e.*, ON-state) and plotted with respect to TNF-α concentration (*n*) in Figure 6 (c). Figure 6 (c) shows that the $R-n$ relationships measured from multiple sensors exhibit a high degree of device-to-device consistency and can serve as a standard curve for TNF-α quantification. These $R-n$ relationships can be well fitted with Langmuir isotherm, and the equilibrium constant of the antibody-(TNF-α) pair was extracted to be K_D = 308 ± 33 fM. These device demonstrations have preliminarily demonstrated that NASE can produce multilayer TMDC device components with a good uniformity of electronic properties. In addition, it should be noted that our MoS_2 FET biosensors exhibit a very low limit-of-detection (LOD) (not higher than 60 fM). Such a fM-level LOD would potentially enable new bioassay chips offering single-molecule-level analysis capabilities.

We have experimentally demonstrated the production of multilayer structures with microscale lateral dimensions using NASE. To further evaluate the scalability of NASE for generating atomically layered structures with nanoscale lateral dimensions, we performed a molecular dynamics (MD) simulation of the NASE processes for exfoliating nanoscale-lateral-size layered structures. In this simulation work, we specifically simulated the shear exfoliation of few-layer-graphene nanostructures into PS fixing layers, because few-layer-graphene has the simpler crystal structure than TMDCs, which can simplify our simulation, but graphene layers exhibit mechanical properties very similar to most TMDCs. Figure 7 shows the simulation results of the

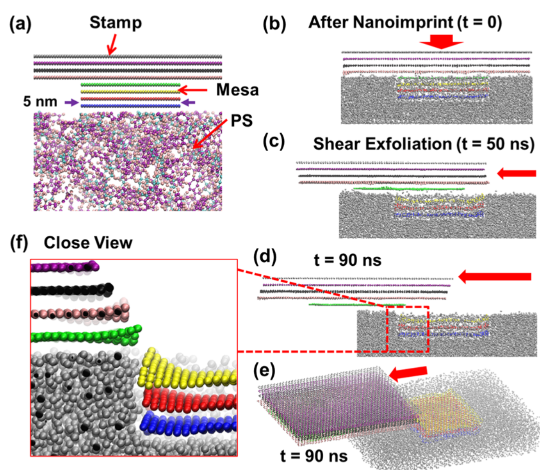

Figure 7. Molecular dynamics (MD) simulation of the NASE process for exfoliating atomically layered nanostructures: (a) a selected part of the 3-D simulation region, showing the cross-sectional view of the initial configuration of the NASE process, involving a graphite stamp bearing 5 nm size, 4-layer mesas and a PS fixing layer; (b–d) cross-sectional snapshots of the MD simulation result of a postnanoimprint shear exfoliation course at $t = 0, 50, 90$ ns; (e) a 3-D snapshot of the simulated system at $t = 90$ ns; (f) a zoom-in view of the imprinted PS well bearing graphene layers, especially displaying the interface between the edges of exfoliated layers and the sidewall of the imprinted PS well.

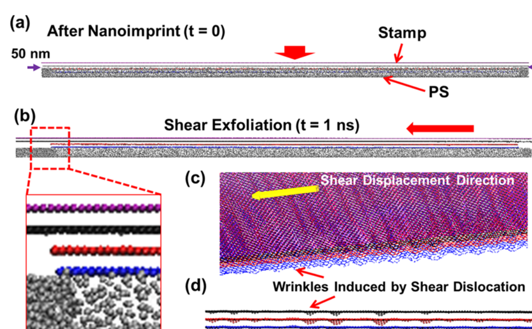

Figure 8. Molecular dynamics (MD) simulation of the NASE process for exfoliating relatively low-aspect-ratio layered structures: (a) a cross-sectional snapshot of the NASE stage, in which a graphite stamp bearing 50 nm size, bilayer mesas has been imprinted into a PS fixing layer (*i.e.*, $t = 0$); (b) a cross-sectional snapshot of the postnanoimprint shear exfoliation course taken at $t = 1$ ns; (c) and (d) are tilted and side views, respectively, of a 3-D snapshot of the simulated system at $t = 1$ ns, which exhibits wrinkle features induced by the shear dislocation process.

NASE process for exfoliating 5 nm size, 4-layer graphene mesas into a PS layer. In particular, Figure 7 (b–e) display a set of snapshots of the simulated postnanoimprint shear exfoliation stages at selected times ($t = 0$, 50, 90 ns). These dynamic simulation results show that at least three layers from a mesa can be reliably exfoliated and trapped into the imprinted PS well, whereas the layer closest to the top edge of the PS well (*i.e.*, the green layer shown in Figure 7) exhibits a significant probability to be dislocated out of the PS well. Figure 7 (f) shows a zoom-in view of the interface between the graphene layer edges and the sidewall of the imprinted PS well. From Figure 7 (f), it can be observed that the imprinted well is deep enough to prevent the trapped graphene layers from sliding over one another. This guarantees that the imprinted/exfoliated multiple layers can retain their original AB-stacking mode after a NASE process. These MD simulation results imply that NASE could be potentially used for generating high-quality nanoscale-lateral-size layered device structures. More details about the MD simulation setup are described in the Materials and Methods. In addition, a dynamic animation of the whole NASE process for exfoliating 5 nm size, 4-layer few-layer-graphene mesas is presented as a Supporting Information document.

We also used MD simulations to investigate the effects of the geometric dimensions of prestructured stamping structures on the resultant morphology of NASE-produced layered nanostructures. For example, we simulated the NASE process for exfoliating relatively low-aspect-ratio graphene nanostructures (*i.e.*, 50 nm size, bilayer graphene mesas prestructured on a stamp), as shown in Figure 8. Specifically, Figure 8 (a) and (b) display two cross-sectional snapshots of the postnanoimprint shear exfoliation course taken at $t = 0$ and 1 ns, respectively. Figure 8 (b) shows that the imprinted bilayer mesa is pulled out of the imprinted PS by the bulk stamp moving along a shear direction, and the imprinted PS well fails to immobilize such low-aspect-ratio structures. This can be attributed to the fact that the layered structures with a lower aspect-ratio possess much lower bending rigidity than the ones with a higher aspect-ratio, because the bending rigidity of a solid flake can be expressed as $Eh^3/12(1 - v^2)$, where E, h, and v are the Young's modulus, thickness, and Poisson's ratio of the flake. Therefore, relatively low-aspect-ratio layered structures can easily deform under the shear stress exerted by the bulk stamp, and therefore they can be easily pulled out of the imprinted well. Our simulation shows that the initial form of such shear-stress-induced deformation in exfoliated mesa layers is a set of nanoscale wrinkles. Figure 8 (c) and (d) display the tilted and side views, respectively, of a 3-D snapshot of the low-aspect-ratio graphene layers at $t = 1$ ns, which exhibits a set of wrinkle features induced by the shear dislocation process. Such wrinkle features do not appear in relatively high-aspect-ratio layered nanostructures (*e.g.*, 5 nm size, 4-layer mesas shown in Figure 7) due to their large in-plane stiffness. In addition, our simulations indicate that the large deformations created in relatively low-aspect-ratio layered structures can reduce the cohesive energies of graphene/graphene as well as graphene/PS interfaces, and further enhance the occurring probability of the detachment of imprinted/exfoliated layers from the PS fixing layer. Therefore, our MD simulation results, consistent with our experimental results, also suggest that NASE is more suitable for producing uniform multilayer structures

with relatively high aspect-ratios than to producing monolayer/few-layer structures with relatively low aspect-ratios. However, as mentioned above, NASE-produced multilayer structures with uniform initial thicknesses could be further trimmed to the thinner thicknesses by using established layer-thinning approaches.[32,33] As discussed above, in a real NASE process, when a MoS_2 stamp is sheared horizontally, a vertical pressure is applied to the stamp to avoid the ripple formation. The relationship between the flake rigidity and the required vertical pressure is qualitatively discussed in the Supporting Information.

CONCLUSION

In conclusion, we present a top-down nanofabrication approach, termed as nanoimprint-assisted shear exfoliation (NASE), which is capable of producing high-quality multilayer MoS_2 structures with a good uniformity of feature thicknesses as well as electronic properties. NASE uniquely combines the nanoimprinting and shear exfoliation of prestructured layered nano/microstructures into polymeric fixing layers. Our experiments demonstrate that such a NASE mechanism can result in high-quality 40–200 nm high, 10–15 μm size MoS_2 flake arrays with a high uniformity of flake thicknesses (*i.e.*, relative thickness error ~12%) over cm^2-scale areas, which surpasses the performance of previously reported exfoliation methods for generating layered materials, in terms of large-area ordering and thickness uniformity of exfoliated structures. We have demonstrated the fabrication of working FET arrays and FET-based label-free biosensors with NASE-produced multilayer MoS_2 channels. These functional devices exhibit very consistent performance, and the characterization data measured from these devices show that NASE-produced MoS_2 flakes have a good uniformity of electronic properties. Especially, our FET-based biosensors exhibit a high device-to-device consistency in the sensor responses to specific analyte biomolecules. Using multiple such biosensors, we have preliminarily demonstrated quantification of standard curves for fM-level cell-signaling protein detection as well as antigen–antibody affinity properties. Furthermore, our MD simulation results of NASE processes suggest that the presented shear-exfoliation mechanism could be further developed for generating nanoscale-lateral-size layered structures for meeting the ever-evolving demands for device miniaturization. Such a MD simulation model also provides critical information for understanding the effects of the geometric dimensions of prestructured stamping structures on the resultant morphology of NASE-produced layered nanostructures. This work advances critical nanofabrication/nanomanufacturing knowledge toward ultimately realizing upscalable production of highly uniform MoS_2 device arrays. The presented NASE approach holds significant potential to leverage the superior properties of MoS_2 and other emerging TMDCs for practical scale-up device applications.

MATERIALS AND METHODS

Fabrication of MoS_2 Stamps. The bulk MoS_2 ingots for making NASE stamps were purchased from SPI, Inc. The ingot size is ~1 cm^2. An as-purchased MoS_2 ingot is usually not flat and its surface is noticeably oxidized or contaminated. Before making a MoS_2 stamp, we used a scotch tape to mechanically peel off several upper layers to obtain a pristine MoS_2 surface and also improve the flatness of the sample. After each peeling process, we observed the evolution of terrace edges on the sample surface, aiming to obtain a sample with the minimal number of terrace edges. Such terrace edges are responsible for the thickness nonuniformity of imprinted PS films (Figure 3 (a)) and exfoliated multilayer MoS_2 flakes (Figure 3 (c)), and sometime result in exfoliation of unwanted MoS_2 structures. Our future work will seek to create new preparation methods for further improving the flatness of MoS_2 ingots and the yield of NASE processes. The prepatterning of bulk MoS_2 stamps was performed using a method previously reported by us.[26] In particular, the protrusive mesa structures on MoS_2 stamps were formed by using SF_6 reactive ion etching (RIE) (RIE parameters: SF_6, flow rate: 20 sccm, chamber pressure: 20 mTorr, RF power: 200 W). The etching rate of this RIE receipt was measured to be ~100 nm/min in our RIE tool (Plasma-Therm790).

Thermal NIL of Prestructured MoS_2 Structures into PS Fixing Layers. A 50–60 nm thick polystyrene (PS) layer was coated on a SiO_2/Si substrate, which was precleaned by using standard RCA cleaning processes. A bulk MoS_2 stamp was attached on a piece of Si wafer using double-sided tape and subsequently pressed to the PS-coated SiO_2/Si substrate by using a homemade thermal nanoimprint tool that can generate a gauge pressure as large as 3 MPa. The thermal NIL process was performed at $T = 140$ °C for 10 min, which was followed with a cooling process. Afterward, the MoS_2 stamp/substrate system was transferred onto our motorized roller system for performing the shear exfoliation.

Setup and Operation of the Lab-Made Motorized Roller Tool for Generating Shear Exfoliation. Figure 2 (a) shows our lab-made motorized roller tool. The main roller (diameter: 60 mm; width: 150 mm) is responsible for generating the relative shear displacement between a stamp/substrate pair. It was made of aluminum alloy and coated with a 3 mm thick urethane rubber layer to provide a conformal contact between the roller and the flat sample holder as well as enhance the friction between the roller and the stamp (or the substrate). The vertical stage can generate adjustable gauge pressure (or force) between the roller and the flat sample holder (or between the MoS_2 stamp and the imprinted substrate). In a typical NASE process, this vertical force is adjusted to be ~200 N. The roller is driven by a brushless motor (USM425–401W from Oriental Motor U.S.A. CORP.), which is coupled with an electric speed controller (USP425–1U from Oriental Motor U.S.A. CORP.) to provide continuous variation of rotation speed. The web speed measured at the roller surface can be controlled within a range of 0 to 30 mm/sec. In a typical NASE process, this speed is adjusted to be ~1 mm/sec, and the typical operation time for a shear exfoliation cycle is 1–5 s.

Raman and AFM Characterizations. The Raman spectra of NASE-produced MoS_2 flakes were measured using a Renishaw inVia microscope equipped with a 633 nm laser. The surface topography of MoS_2 flakes was characterized using a Veeco Dimension Icon Atomic Force Microscope.

Fabrication and Characterization of Arrays of Back-Gated MoS_2 FETs. To make a working FET array, a SiO_2-coated p^+-Si substrate

ARTICLE

bearing NASE-produced multilayer MoS_2 flakes was first etched by O_2 plasma, and the PS regions not covered by MoS_2 flakes were completely removed. There were residual PS layers under MoS_2 flakes, which were estimated to be thinner than 5 nm. Afterward, all MoS_2 flakes were thinned from 50 to 100 nm to ∼20 nm by using SF_6 plasma (power: 40 W; precursor flow rate: 10 sccm; pressure 10 mTorr; etching rate: ∼ 20 nm/min). The effect of this plasma recipe on various FET parameters was studied through comparing the transfer characteristics of MoS_2 FETs measured before and after their MoS_2 channels were thinned by plasma. The details of this discussion can be found in the Supporting Information. After this thinning process, the drain (D) and source (S) contacts of the FET array were fabricated using photolithography followed with metal deposition (5 nm Ti and 50 nm Au) and lift-off in a solvent. The p^+-Si substrate was used as the common back gate, and the thermally grown SiO_2 layer (300 nm thick) served as the gate dielectric (the effective gate dielectric for a FET also includes a residual PS layer). All FET characteristic curves were measured at the room temperature by using an HP-4145B semiconductor parameter analyzer, which was connected to a LakeShore probe station.

Fabrication, Functionalization, and Characterization of MoS_2 FET Biosensors. To convert a MoS_2 FET into a biosensor for detecting TNF-α molecules, we first need to passivate its D/S contact electrodes to eliminate the effect of antibody−antigen binding on the contact resistances between D/S contacts and the MoS_2 channel. In this work, we used patterned photoresist layers (∼2 μm thick SU8) to fully cover and passivate D/S contacts. Figure S5 (a) in the Supporting Information shows an optical micrograph of a representative MoS_2 FET biosensor, in which the D/S contacts are passivated by photoresist layers. After the electrode passivation, the multilayer MoS_2 channel needs to be functionalized with antihuman TNF-α antibody receptors. Figure S5 (b) illustrates the antibody functionalization protocol used in this work, which includes (1) incubating MoS_2 FETs into a 5% (3-Aminopropyl) triethoxysilane (APTES) solution (from Sigma-Aldrich Co. LLC.) for 1 h; (2) incubating the MoS_2 channels silanized with APTES in a 5% solution of glutaraldehyde (GA, from Sigma-Aldrich Co. LLC.) in phosphate buffered saline (PBS) for 2 h; (3) incubating FETs in an antihuman TNF-α antibody solution for 1 h; and (4) TNF-α detection. Specifically, for Step (4) TNF-α detection, we perform the following steps: (a) incubate an as-functionalized FET sensor in a target TNF-α solution (solvent: 1×PBS) for 20−30 min to ensure that the (TNF-α)-antibody association/dissociation reaction reach to the equilibrium state; (b) rinse away unreacted TNF-α molecules with DI water; (c) blow dry the sensor and measure its transfer characteristics using a semiconductor analyzer.

It should be noted that although our as-fabricated MoS_2 FETs can be characterized in a relatively dense array (device spacing could be as small as 10−15 μm), as shown in Figure 5 (b), our current FET biosensors have to be characterized in a much more dispersed array configuration (device-to-device spacings: 3−5 mm), because extra space is needed by each sensor for hosting liquid droplets of target solutions as well as passivated large electrodes. However, this issue is anticipated to be addressed by integrating additional microfluidic structures for confining analyte solutions to individual sensors in the future.

Molecular Dynamics Simulation. Our MD simulations were performed using the large-scale atomic/molecular massively parallel simulator (LAMMPS) software package that was developed at Sandia National Laboratories. In our simulations, each graphene layer was modeled using an adaptive interatomic reactive empirical bond order (AIREBO) potential function,[41] while the carbon−carbon interaction between two graphene layers was modeled by a registry-dependent potential.[42] With this setup, we obtained in-plane carbon−carbon distance of 1.401 Å, equilibrium interlayer spacing of 3.365 Å in AB stacking, cohesion energy of 45.2 meV per atom with respect to one graphene layer (*i.e.*, cleavage energy per atom), and interlayer shear modulus of 5.01 GPa (C_{44}) and intralayer shear modulus of 38.8 GPa (C_{33}). For the description of the intermolecular and intramolecular interactions in polystyrene (PS), we used the optimized potentials for liquid simulation (OPLS) force field.[43] A three-stage energy minimization and isobaric−isothermal simulation of the bulk PS system provided us with a density of 1005 kg/m^3. Afterward, we placed few-layer graphene flakes at a distance of 2.5 Å above the bulk polystyrene and adopted the conjugate gradient method to perform the energy minimization of the system before initiating the MD integration, as shown in Figure 7 (a). A 12 Å cutoff radius was applied for Coulomb and van der Waals interactions. The electrostatic interactions were treated by using the particle−particle particle−mesh (PPPM) method with a precision of 10^{-4}. The dielectric constant was set to 1. Periodic boundaries were applied in x and y directions during the simulations. This is consistent with our NASE setup for generating periodic layered structures. A Verlet time-integration scheme was applied throughout the whole simulation. Following the initial setup shown in Figure 1 (a), the PS layer was subjected to a 10 ns isothermal ensemble at T = 500 K, using the Nose−Hoover thermostat. This ensemble simulated the thermal nanoimprint step of the NASE process. After this step, the few-layer graphene mesas were fully imprinted into the PS layer, as shown in Figure 7 (b). After the thermal nanoimprint step, the well-equilibrated configuration was obtained by cooling down the system from T = 500 K to room temperature at 1 bar using the NPT simulation with the set temperature T lowered by 10 K every 10 ns (effective cooling rate 1 K/ns). In the following simulations of shear exfoliation of imprinted few-layer graphene structures, the topmost layers of all few-layer graphene mesas and 2 Å of the PS layer from the bottom were set as rigid. To fully mimic the experimental setup, the topmost mesa layer was pulled away along a shear direction (*i.e.*, x-axis direction) with speed of 2×10^{-4} Å/ps, which corresponds to the web speed of our 60 mm-diameter roller rotating at an angular speed of ∼6 rpm.

Conflict of Interest: The authors declare no competing financial interest.

Acknowledgment. The NASE technology is supported by the NSF grant # CMMI-1232883. The biosensing work is supported by the NSF grant # ECCS-1452916. The authors would like to thank the staff of the Univeristy of Michigan's North Campus Electron Microbeam Analysis Laboratory for providing the support of material characterization and thank the staff of the University of Michigan's Lurie Nanofabrication Facility for providing the support of device fabrication.

Supporting Information Available: The Supporting Information is available free of charge on the ACS Publications website at DOI: 10.1021/acsnano.5b01715.

Transfer characteristics of 45 back-gated field-effect transistors (FETs) made from NASE-produced MoS_2 flakes (Figure S1); the optical micrograph of two representative back-gated FETs made from selected NASE-produced multilayer MoS_2 flakes free of residual PS (Figure S2); transfer characteristics of 11 back-gated FETs made from NASE-produced multilayer MoS_2 flakes free of residual PS (Figure S3); statistics of the FET performance parameter data measured from 11 FETs made from NASE-produced MoS_2 flakes free of residual PS (Figure S4); passivation and functionalization of MoS_2 biosensors (Figure S5); comparison of transfer characteristics of a MoS2 FET measured before and after plasma thinning (text and Figure S6); discussion on relationship between flake rigidity and required vertical pressure (text and Figure S7). (PDF)

Video showing a shear exfoliation process driven by a motorized roller tool. (AVI)

Animation of the molecular dynamics (MD) simulation of the NASE process for exfoliating 5 nm size, 4-layer graphene nanostructures into a PS fixing layer. (MPG)

REFERENCES AND NOTES

1. Radisavljevic, B.; Radenovic, A.; Brivio, J.; Giacometti, V.; Kis, A. Single-Layer MoS_2 Transistors. *Nat. Nanotechnol.* **2011**, *6*, 147–150.
2. Mak, K. F.; Lee, C.; Hone, J.; Shan, J.; Heinz, T. F. Atomically Thin MoS_2: A New Direct-Gap Semiconductor. *Phys. Rev. Lett.* **2010**, *105*, 136805/1–136805/15.

3. Korn, T.; Heydrich, S.; Hirmer, M.; Schmutzler, J.; Schüller, C. Low-Temperature Photocarrier Dynamics in Monolayer MoS_2. *Appl. Phys. Lett.* **2011**, *99*, 102109/1–102109/3.
4. Chhowalla, M.; Shin, H. S.; Eda, G.; Li, L.-J.; Loh, K. P.; Zhang, H. The Chemistry of Two-Dimensional Layered Transition Metal Dichalcogenide Nanosheet. *Nat. Chem.* **2013**, *5*, 263–275.
5. Wang, H.; Yu, L.; Lee, Y.-H.; Shi, Y.; Hsu, A.; Chin, M. L.; Li, L.-J.; Dubey, M.; Kong, J.; Palacios, T. Integrated Circuits Based on Bilayer MoS_2 Transistors. *Nano Lett.* **2012**, *12*, 4674–4680.
6. Chang, H. Y.; Yang, S. X.; Lee, J. H.; Tao, L.; Hwang, W. S.; Jena, D.; Lu, N. S.; Akinwande, D. High-Performance, Highly Bendable MoS_2 Transistors with High-K Dielectrics for Flexible Low-Power Systems. *ACS Nano* **2013**, *7*, 5446–5452.
7. Radisavljevic, B.; Kis, A. Mobility Engineering and A Metal–Insulator Transition in Monolayer MoS_2. *Nat. Mater.* **2013**, *12*, 815–820.
8. He, Q.; Zeng, Z.; Yin, Z.; Li, H.; Wu, S.; Huang, X.; Zhang, H. Fabrication of Flexible MoS_2 Thin-Film Transistor Arrays for Practical Gas-Sensing Applications. *Small* **2012**, *8*, 2994–2999.
9. Wang, L.; Wang, Y.; Wong, J. I.; Palacios, T.; Kong, J.; Yang, H. Y. Functionalized MoS_2 Nanosheet-Based Field-Effect Biosensor for Label-Free Sensitive Detection of Cancer Marker Proteins in Solution. *Small* **2014**, *10*, 1101–1105.
10. Sarkar, D.; Liu, W.; Xie, X. J.; Anselmo, A. C.; Mitragotri, S.; Banerjee, K. MoS_2 Field-Effect Transistor for Next-Generation Label-Free Biosensors. *ACS Nano* **2014**, *8*, 3992–4003.
11. Yin, Z.; Li, H.; Li, H.; Jiang, L.; Shi, Y.; Sun, Y.; Lu, G.; Zhang, Q.; Chen, X.; Zhang, H. Single-Layer MoS_2 Phototransistors. *ACS Nano* **2011**, *6*, 74–80.
12. Chen, M.; Nam, H.; Wi, S.; Priessnitz, G.; Gunawan, I. M.; Liang, X. Multibit Data Storage States Formed in Plasma-Treated MoS_2 Transistors. *ACS Nano* **2014**, *8*, 4023–4032.
13. Wi, S.; Kim, H.; Chen, M.; Nam, H.; Guo, L. J.; Meyhofer, E.; Liang, X. Enhancement of Photovoltaic Response in Multilayer MoS_2 Induced by Plasma Doping. *ACS Nano* **2014**, *8*, 5270–5281.
14. Shanmugam, M.; Durcan, C. A.; Yu, B. Layered Semiconductor Molybdenum Disulfide Nanomembrane Based Schottky-Barrier Solar Cells. *Nanoscale* **2012**, *4*, 7399–7405.
15. Wi, S.; Chen, M.; Nam, H.; Liu, A. C.; Meyhofer, E.; Liang, X. High Blue-Near Ultraviolet Photodiode Response of Vertically Stacked Graphene-MoS_2-Metal Heterostructures. *Appl. Phys. Lett.* **2014**, *104*, 232103/1–232103/5.
16. Xiao, D.; Liu, G. B.; Feng, W. X.; Xu, X. D.; Yao, W. Coupled Spin and Valley Physics in Monolayers of MoS_2 and Other Group-VI Dichalcogenides. *Phys. Rev. Lett.* **2012**, *108*, 196802/1–196802/5.
17. Jiang, T.; Liu, H.; Huang, D.; Zhang, S.; Li, Y.; Gong, X.; Shen, Y. R.; Liu, W. T.; Wu, S. Valley and Band Structure Engineering of Folded MoS_2 Bilayers. *Nat. Nanotechnol.* **2014**, *9*, 825–829.
18. Wang, J.; Lundstrom, M. Does Source-to-Drain Tunneling Limit The Ultimate Scaling of MOSFETs? *International Electron Devices 2002 Meeting, Technical Digest*; IEEE: New York, **2002**; pp 707–710.
19. Zhan, Y.; Liu, Z.; Najmaei, S.; Ajayan, P. M.; Lou, J. Large-Area Vapor-Phase Growth and Characterization of MoS_2 Atomic Layers on a SiO_2 Substrate. *Small* **2012**, *8*, 966–971.
20. Lee, Y. H.; Zhang, X. Q.; Zhang, W.; Chang, M. T.; Lin, C. T.; Chang, K. D.; Yu, Y. C.; Wang, J. T. W.; Chang, C. S.; Li, L. J. Synthesis of Large-Area MoS_2 Atomic Layers with Chemical Vapor Deposition. *Adv. Mater.* **2012**, *24*, 2320–2325.
21. Huang, J.-K.; Pu, J.; Hsu, C.-L.; Chiu, M.-H.; Juang, Z.-Y.; Chang, Y.-H.; Chang, W.-H.; Iwasa, Y.; Takenobu, T.; Li, L.-J. Large-Area Synthesis of Highly Crystalline WSe_2 Monolayers and Device Applications. *ACS Nano* **2013**, *8*, 923–930.
22. Fontana, M.; Deppe, T.; Boyd, A. K.; Rinzan, M.; Liu, A. Y.; Paranjape, M.; Barbara, P. Electron-Hole Transport and Photovoltaic Effect in Gated MoS_2 Schottky Junctions. *Sci. Rep.* **2013**, *3*, 1634/1–1634/5.
23. Kim, S.; Konar, A.; Hwang, W. S.; Lee, J. H.; Lee, J.; Yang, J.; Jung, C.; Kim, H.; Yoo, J. B.; Choi, J. Y.; *et al.* High-Mobility and Low-Power Thin-Film Transistors Based on Multilayer MoS_2 Crystals. *Nat. Commun.* **2012**, *3*, 1011/1–1011/7.
24. Das, S.; Chen, H. Y.; Penumatcha, A. V.; Appenzeller, J. High Performance Multilayer MoS_2 Transistors with Scandium Contacts. *Nano Lett.* **2013**, *13*, 100–105.
25. Liang, X.; Fu, Z.; Chou, S. Y. Graphene Transistors Fabricated *via* Transfer-Printing in Device Active-Areas on Large Wafer. *Nano Lett.* **2007**, *7*, 3840–3844.
26. Nam, H.; Wi, S.; Rokni, H.; Chen, M.; Priessnitz, G.; Lu, W.; Liang, X. MoS_2 Transistors Fabricated *via* Plasma-Assisted Nanoprinting of Few-Layer MoS_2 Flakes into Large-Area Arrays. *ACS Nano* **2013**, *7*, 5870–5881.
27. Chou, S. Y.; Krauss, P. R.; Renstrom, P. J. Imprint of Sub-25 nm Vias AND Trenches in Polymers. *Appl. Phys. Lett.* **1995**, *67*, 3114–3116.
28. Liang, X.; Chang, A. S. P.; Zhang, Y.; Harteneck, B. D.; Choo, H.; Olynick, D. L.; Cabrini, S. Electrostatic Force Assisted Exfoliation of Prepatterned Few-Layer Graphenes into Device Sites. *Nano Lett.* **2009**, *9*, 467–472.
29. Sidorov, A. N.; Yazdanpanah, M. M.; Jalilian, R.; Ouseph, P. J.; Cohn, R. W.; Sumanasekera, G. U. Electrostatic Deposition of Graphene. *Nanotechnology* **2007**, *18*, 135301/1–135301/4.
30. Isshiki, T.; Nishio, K.; Saijo, H.; Shiojiri, M.; Yabuuchi, Y.; Takahashi, N. High-Resolution Transmission Electron Microscopy of Hexagonal and Rhombohedral Molybdenum Disulfide Crystals. *Microsc. Res. Tech.* **1993**, *25*, 325–334.
31. Shiojiri, M.; Isshiki, T.; Saijo, H.; Yabuuchi, Y.; Takahashi, N. Cross-Sectional Observations of Layer Structures and Stacking Faults in Natural and Synthesized Molybdenum Disulfide Crystals by High-Resolution Transmission Electron Microscopy. *J. Electron Microsc.* **1993**, *42*, 72–78.
32. Liu, Y. L.; Nan, H. Y.; Wu, X.; Pan, W.; Wang, W. H.; Bai, J.; Zhao, W. W.; Sun, L. T.; Wang, X. R.; Ni, Z. H. Layer-by-Layer Thinning of MoS_2 by Plasma. *ACS Nano* **2013**, *7*, 4202–4209.
33. Castellanos-Gomez, A.; Barkelid, M.; Goossens, A. M.; Calado, V. E.; van der Zant, H. S. J.; Steele, G. A. Laser-Thinning of MoS_2: On Demand Generation of a Single-Layer Semiconductor. *Nano Lett.* **2012**, *12*, 3187–3192.
34. Li, H.; Yin, Z. Y.; He, Q. Y.; Li, H.; Huang, X.; Lu, G.; Fam, D. W. H.; Tok, A. I. Y.; Zhang, Q.; Zhang, H. Fabrication of Single- and Multilayer MoS_2 Film-Based Field-Effect Transistors for Sensing NO at Room Temperature. *Small* **2012**, *8*, 63–67.
35. Fiori, G.; Szafranek, B. N.; Iannaccone, G.; Neumaier, D. Velocity Saturation in Few-Layer MoS_2 Transistor. *Appl. Phys. Lett.* **2013**, *103*, 233509/1–233509/4.
36. Bao, W. Z.; Cai, X. H.; Kim, D.; Sridhara, K.; Fuhrer, M. S. High Mobility Ambipolar MoS_2 Field-Effect Transistors: Substrate and Dielectric Effects. *Appl. Phys. Lett.* **2013**, *102*, 042104/1–042104/3.
37. Li, H.; Zhang, Q.; Yap, C. C. R.; Tay, B. K.; Edwin, T. H. T.; Olivier, A.; Baillargeat, D. From Bulk to Monolayer MoS_2: Evolution of Raman Scattering. *Adv. Funct. Mater.* **2012**, *22*, 1385–1390.
38. Lee, C.; Yan, H.; Brus, L. E.; Heinz, T. F.; Hone, J.; Ryu, S. Anomalous Lattice Vibrations of Single-and Few-Layer MoS_2. *ACS Nano* **2010**, *4*, 2695–2700.
39. Zhang, Y.; Ye, J.; Matsuhashi, Y.; Iwasa, Y. Ambipolar MoS_2 Thin Flake Transistors. *Nano Lett.* **2012**, *12*, 1136–1140.
40. Liang, X. G.; Giacometti, V.; Ismach, A.; Harteneck, B. D.; Olynick, D. L.; Cabrini, S. Roller-Style Electrostatic Printing of Prepatterned Few-Layer-Graphenes. *Appl. Phys. Lett.* **2010**, *96*, 013109/1–013109/3.
41. Brenner, D. W.; Shenderova, O. A.; Harrison, J. A.; Stuart, S. J.; Ni, B.; Sinnott, S. B. A Second-Generation Reactive Empirical Bond Order (REBO) Potential Energy Expression for Hydrocarbons. *J. Phys.: Condens. Matter* **2002**, *14*, 783–802.

42. Kolmogorov, A. N.; Crespi, V. H. Registry-Dependent Interlayer Potential for Graphitic Systems. *Phys. Rev. B: Condens. Matter Mater. Phys.* **2005**, *71*, 235415/1–235415/6.
43. Jorgensen, W. L.; Maxwell, D. S.; TiradoRives, J. Development and Testing of The OPLS All-Atom Force Field on Conformational Energetics and Properties of Organic Liquids. *J. Am. Chem. Soc.* **1996**, *118*, 11225–11236.